Tropical cyclone-induced periodical positioning disturbances during the 2017 Hato in the Hong Kong region

Shiwei YU[1,2], Zhizhao LIU[1,2]*

[1]Department of Land Surveying and Geo-Informatics, The Hong Kong Polytechnic University, 11 Yuk Choi Road, Hung Hom, Kowloon, Hong Kong, P.R. China

[2]Research Institute for Sustainable Urban Development, The Hong Kong Polytechnic University, 11 Yuk Choi Road, Hung Hom, Kowloon, Hong Kong, P.R. China

Tel: (852)2766 5961 Fax: (852)2330 2994

Corresponding author: Zhizhao Liu, lszzliu@polyu.edu.hk

ORCID: Zhizhao Liu, 0000-0001-6822-9248

ORCID: Shiwei YU, 0000-0002-8258-7241

Abstract The tropospheric delay is an important error source in the Global Positioning System (GPS) positioning and navigation applications. Although most of the tropospheric delays can be removed in the double-differencing (DD) positioning mode, their remaining residuals can still contaminate the positioning accuracy and become unpredictable when tropospheric condition encounters severe variations such as during a tropical cyclone (TC) event. We investigated the positioning performance of five baselines with lengths ranging from 7.8 km to 49.9 km during the 2017 TC Hato. The results showed that the TC Hato brought a significant disturbance to the GPS baseline positioning results, particularly in the vertical (up) component. The TC Hato started to affect Hong Kong and the root mean squares (RMS) of GPS positioning errors increased dramatically from about 30 mm to 140 mm. when it was at a distance of 400–600 km from Hong Kong on August 22, 2017. We found that the vertical positioning errors on that day have the major periods: 2.7 h, 3.0 h, 3.4 h, 4.0 h, and 4.8 h. Examining the wet and hydrostatic parts of the tropospheric delays via the continuous wavelet spectral analysis, we found that the periodical variation of the positioning results on August 22 was caused by the periodical variation of the precipitable water vapor (PWV). The variation of differenced PWV between two baseline stations had consistent periods of 2-5 h. Besides, the periods of differenced PWV time series are in good agreement with the spiral rainband in the TC. This finding suggests that the TC Hato induce periodical PWV variations at two GPS stations of baseline, which resulted in GPS positioning errors of the same periods.

Keywords GPS relative positioning; Precipitable water vapor; Tropical cyclone; Discrete Fourier transform;

Introduction

The accuracy and reliability of the Global Positioning System (GPS) positioning are important topics in the GPS community. One of the factors that affect the accuracy and reliability is the tropospheric effect. GPS signals are delayed and refracted in the troposphere (Chen and Liu 2016). These effects contaminate the positioning results if they are not correctly removed from GPS measurements.

The double-differencing (DD) technology has been widely used in relative positioning models to mitigate the error effects in GPS measurements. In DD observations, the common error sources in GPS measurements, e.g., orbit and clock errors, atmospheric effects, and multipath effect, can be canceled or significantly mitigated, thus improving the positioning performance (Li et al. 2010). However, the tropospheric delays cannot be completely eliminated in DD observations, particularly when two GPS stations in the DD processing experience different tropospheric conditions. This is possible when GPS surveying is made under some particular conditions, such as tropical cyclones (TCs).

A tropical cyclone is a rapidly rotating storm system accompanied by complicated weather, such as powerful winds, heavy rainstorms, and magnificent thunderstorms (Marks 2015). Calori et al. (2016), Chen et al. (2017) and Tunalı and Özlüdemir (2019) have demonstrated that tropospheric delays in GPS signals varied significantly under high-dynamic tropospheric condition. Wilgan et al. (2017) and Zheng et al. (2018) suggested that GPS positioning performance was degraded by unpredictable tropospheric variation. However, the exact relationship between the tropospheric effect and positioning performance is seldom studied during tropical cyclone events.

This study aims to investigate the impact of a super typhoon on the performance of GPS relative positioning. We analyzed the GPS data observed in Hong Kong during the super typhoon Hato (1713), the 13th tropical cyclone over the western North Pacific in 2017. The TC Hato (1713) was a super typhoon and made landfall near Hong Kong with a close distance of about 60 km. It brought massive damages to Hong Kong. At least 129 people were injured, and over 5,300 trees were blown down during the passage of Hato (Hong Kong Observatory 2019). Hong Kong, as a coastal city on the verge of the South China sea, on average, experiences six TCs each year in the past 50 years (Hong Kong Observatory 2019). Thus, it is meaningful to investigate the GPS positioning performance for the region, which often suffers from the impact of tropical cyclones.

In the following sections, the tropical cyclone information and GPS data processing are first introduced. The method based on the discrete Fourier transform is proposed to detect positioning disturbances triggered by the TC Hato. The relationship between positioning disturbances and the tropospheric condition is discussed. In the end, the concluding remarks and findings are summarized.

Data and Methodology

The tropical cyclone Hato (1713) was a super typhoon in 2017, which urged the Hong Kong Observatory (HKO) to issue the highest TC Signal No. 10. On the night of August 20, 2017, a tropical depression formed over the western North Pacific, about 740 km east-southeast of Kaohsiung, Taiwan. On August 22, it intensified into a typhoon after moving through the Luzon Strait. When it approached the Pearl River estuary near Hong Kong on August 23, Hato intensified further and became a super typhoon, the strongest category defined by the HKO, as shown in Table 1. The sustained wind speed near the TC center was estimated to be around 185 km/h on the morning of August 23. After it made landfall over the coast near Macau and Zhuhai, China, at 04:50 UT on August 23, Hato entered western Guangdong, China, and gradually weakened. Finally, Hato moved across Guangxi, China, on August 24, 2017, and dissipated over Yunnan, China, at night (Hong Kong Observatory 2019). The track and strength of Hato are shown in Fig. 1.

Table 1 Classification of the tropical cyclone in km/h as defined by the Hong Kong Observatory (https://www.hko.gov.hk/informtc/class.htm)

Tropical Cyclone Classification	Maximum 10-minute average wind speed near the center
Low (LW)	about 40
Tropical Depression (TD)	41-62
Tropical Storm (TS)	63-87
Severe Tropical Storm (STS)	88-117
Typhoon (T)	118-149
Severe Typhoon (ST)	150-184
Super Typhoon (SuperT)	185

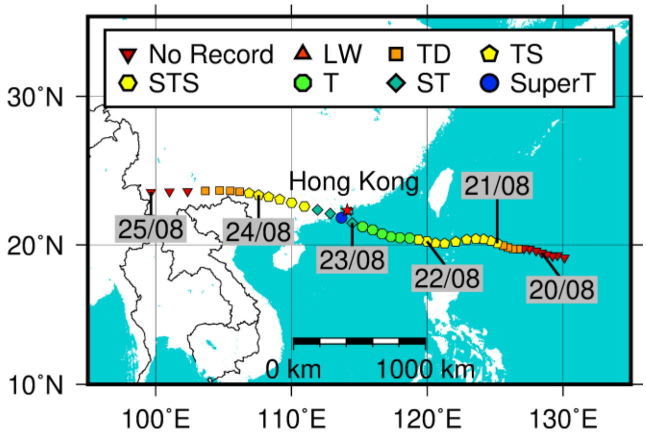

Fig. 1 Track of the tropical cyclone Hato (1713) during August 20-25, 2017. Legends with different colors and shapes represent different categories of the tropical cyclone. The tracking data, from the International Best Track Archive for Climate Stewardship (IBTrACS) of the National Oceanic and Atmospheric Administration (NOAA), were recorded every 3 hours (Knapp et al. 2010)

GPS reference stations in Hong Kong

A network of 18 GPS stations, the Hong Kong Satellite Positioning Reference Station Network (SatRef), has been deployed in Hong Kong since 2000. It has a fairly even distribution of stations, as shown in the top of Fig. 2. The GPS software Bernese (Dach et al. 2015) was utilized to process the GPS data and obtain the reference coordinates of Hong Kong SatRef stations during the TC period of August 16–26, 2017. Five stations from the International Global Navigation Satellite System (GNSS) Services (IGS) network were used as reference stations in the data processing. They are WUH2 in Mainland China, TWTF in Taiwan, PTAG and PIMO in the Philippines, and PBRI in India. Their locations are presented in the bottom of Fig. 2. Then, the reference coordinates of the Hong Kong SatRef stations were obtained by averaging the daily positioning results over the TC period.

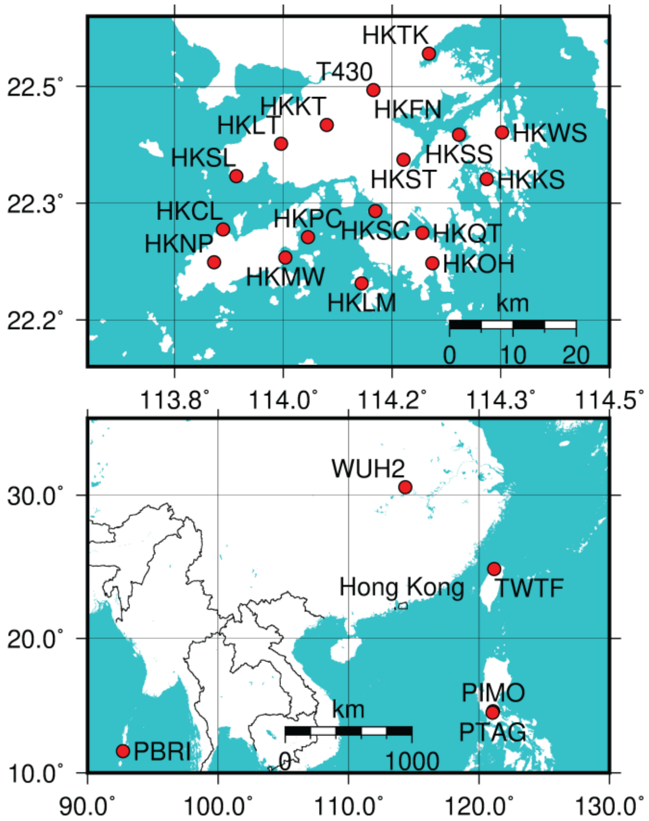

Fig. 2 Location of 18 Hong Kong SatRef GPS stations (top) and five IGS stations (bottom)

Baseline processing models and strategies

To investigate the relative positioning performance in the Hong Kong region during the TC period, we processed the GPS data of Hong Kong SatRef stations in the double-differencing mode with processing strategies shown in Table 2. Five baselines of different lengths were analyzed in this study. They are HKKT-HKLT, HKOH-HKSC, HKKT-HKSS, HKLT-HKWS, and HKNP-HKWS, with a length of 7.8 km, 12.2 km, 20.9 km, 34.9 km, and 49.9 km, respectively. GPS data processing was also based on the ionospheric-free combination observation (L3) to mitigate the ionospheric effect. As the data were processed in a post-mission mode, forward and backward filtering was adopted to get a smoother GPS positioning solution.

Table 2 Summary of GPS data processing

Items	Models and Strategies
Observations	Pseudorange and carrier phase on GPS ionospheric-free combination observation L3
Observation weighting	Elevation-dependent weight

Sampling interval	30 s
Elevation mask angle	10 degrees
Satellite orbit	Fixed using the products from IGS
Satellite clock	Fixed using the products from IGS
Ionospheric delay	First-order effect eliminated by ionospheric-free combination
Tropospheric delay	Estimated with the coordinates
Ambiguity resolve	Estimated as real numbers
Receiver coordinates	Estimated in the kinematic mode

Discrete Fourier transform

In this study, the discrete Fourier transform is used to analyze the GPS positioning errors in the frequency domain. The discrete Fourier transform is a powerful tool to transform signals from the time domain to the frequency domain (Strang 1994). The discrete Fourier transform can be expressed as:

$$X_k = \sum_{n=0}^{N-1} x_n \cdot e^{-\frac{i2\pi}{N}kn} \quad (1)$$

$$e^{-\frac{i2\pi}{N}kn} = \cos(\frac{2\pi}{N}kn) - i \cdot \sin(\frac{2\pi}{N}kn) \quad (2)$$

where x_n is the sequence of the source data at the sampling points of n=0, 1, …, N-1. X_k is the sequence of transformed data with the k=0, 1, …, N-1.

Results and Discussion

An example of applying the discrete Fourier transform to positioning errors is first presented in the following section. The positioning results based on the ionospheric-free combination observation L3 are analyzed in the frequency domain by performing the discrete Fourier transform. After that, the tropospheric effect on the GPS positioning disturbances during the TC Hato (1713) period is discussed.

Example of discrete Fourier transform on the vertical positioning errors

This section shows an example of applying the discrete Fourier transform to the time series of positioning errors. Fig. 3 provides an example of discrete Fourier transform results on the vertical positioning errors for the baseline HKLT-HKWS on August 23, 2017. As shown in thin red curves, the vertical positioning errors fluctuate within the range of ±0.12 m. In addition, three sinusoidal curves with the periods of 6.0 h (720×30 s / 3600 s), 4.0 h (480×30 s / 3600 s), and 2.7 h (320×30 s / 3600 s) are presented together with the positioning errors. The fluctuation of the vertical positioning errors somehow follows the three sinusoidal curves. The corresponding results after performing the discrete Fourier transform on the vertical positioning errors are presented in the right panel. As shown in the ordinate, the spectrum magnitudes represent the significance of the original signal in one certain frequency. Three frequencies at 1/(720×30 s)=4.63×10^{-5} Hz, 1/(480×30 s)=6.94×10^{-5} Hz, and 1/(320×30 s)=1.04×10^{-4} Hz have the largest spectrum magnitudes, as highlighted in red dots. They are consistent with the periods of the three sinusoidal curves in the left panel. It implies that the variation of vertical positioning errors has three primary frequencies at 4.63×10^{-5} Hz, 6.94×10^{-5} Hz, and 1.04×10^{-4} Hz.

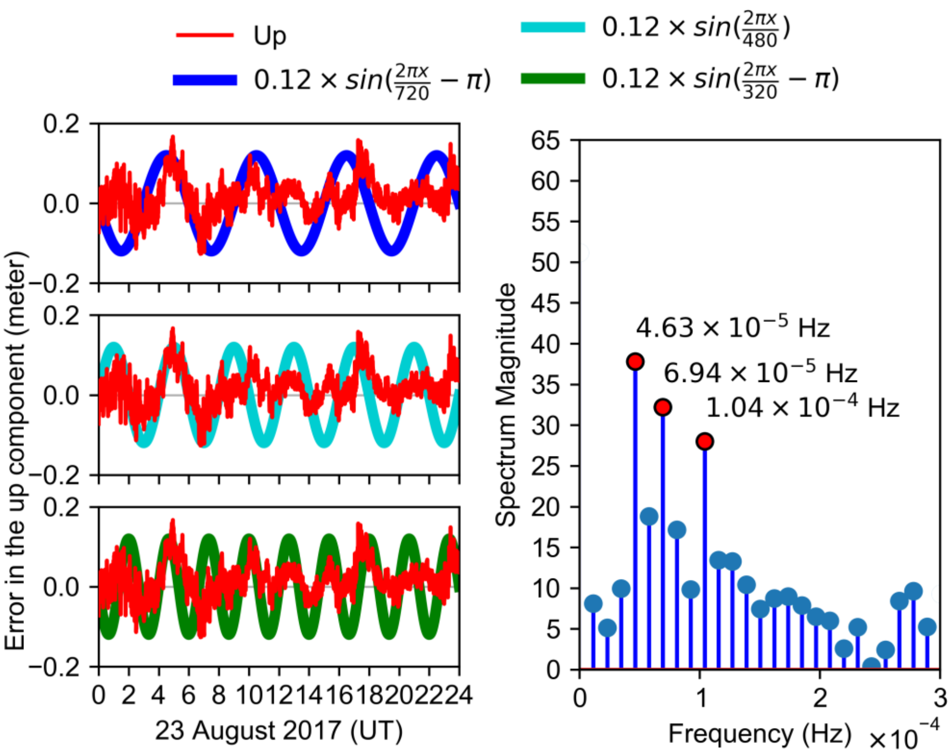

Fig. 3 Positioning errors in the up component for the baseline HKLT-HKWS on August 23, 2017 and the three sinusoidal curves with the periods of 6.0 hours (left top), 4.0 hours (left middle), and 2.7 hours (left bottom), and the corresponding spectrum magnitudes of various frequencies (right) after conducting the discrete Fourier transform on the positioning errors. The three frequencies 1/(6×3600 s)=4.63×10^{-5} Hz, 1/(4×3600 s)=6.94×10^{-5} Hz, and 1/(2.7×3600 s)=1.04×10^{-4} Hz with the largest spectrum magnitudes are highlighted with red dots.

Error! Reference source not found.

Using the same method, the daily discrete Fourier transform results of the vertical error of baseline HKLT-HKWS from August 16 to August 26, 2017, are shown in Fig. 4. It is clear to see that the spectrum magnitudes for frequencies below 1.16×10^{-4} Hz are much larger than those frequencies above 1.16×10^{-4} Hz. This result implies that factors with frequencies lower than the threshold frequency, 1.16(10-4 Hz, affect GPS positioning performance, significantly affect GPS positioning. To find out the exact factors, the spectrum magnitudes of all the frequencies lower than 11.6×10^{-5} Hz, i.e. $(1.16, 2.31, 3.47, 4.63, 5.79, 6.94, 8.10, 9.26, 10.4)\times10^{-5}$ Hz, will be further studied. They correspond to the periods of (24.0, 12.0, 8.0, 6.0, 4.8, 4.0, 3.4, 3.0, 2.7) hours, respectively.

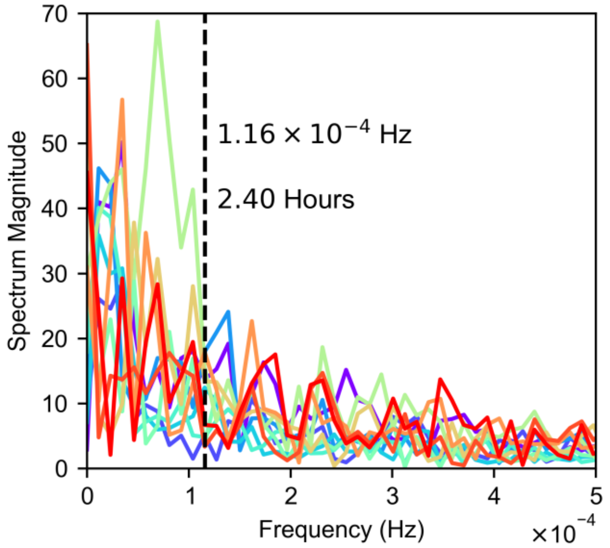

Fig. 4 Spectrum magnitudes of different frequencies from 1.00×10^{-4} Hz to 5.00×10^{-4} Hz based on the discrete Fourier transform of positioning results of baseline HKLT-HKWS in the vertical component. Different colors denote the spectrum magnitudes on different days during August 16-26, 2017. The vertical dashed line denotes the frequency of 1.16×10^{-4} Hz, equivalent to a period of 2.4 hours.

Significant positioning disturbances induced by Hato on August 22

In this section, we investigate the GPS baseline solutions during the TC period. The baseline positioning errors and the distance between the TC center and Hong Kong are presented in Fig. 5. All the positioning errors of the five baselines share the same changing pattern, i.e. a significant variation at the beginning of August 22, 2017. It is also worth noting that the positioning performance was degraded at the beginning of each day from August 16 to August 20. The probable reason for this degradation is the fewer visible satellites. The number of visible satellites with elevation larger than 10º and the geometric dilution of precision (GDOP) from August 16 to August 20 are presented in Fig.

6. The number of visible satellites was just seven between 07:00 UT and 08:00 UT every day and the GDOP had a large value of approximately 4 during this period.

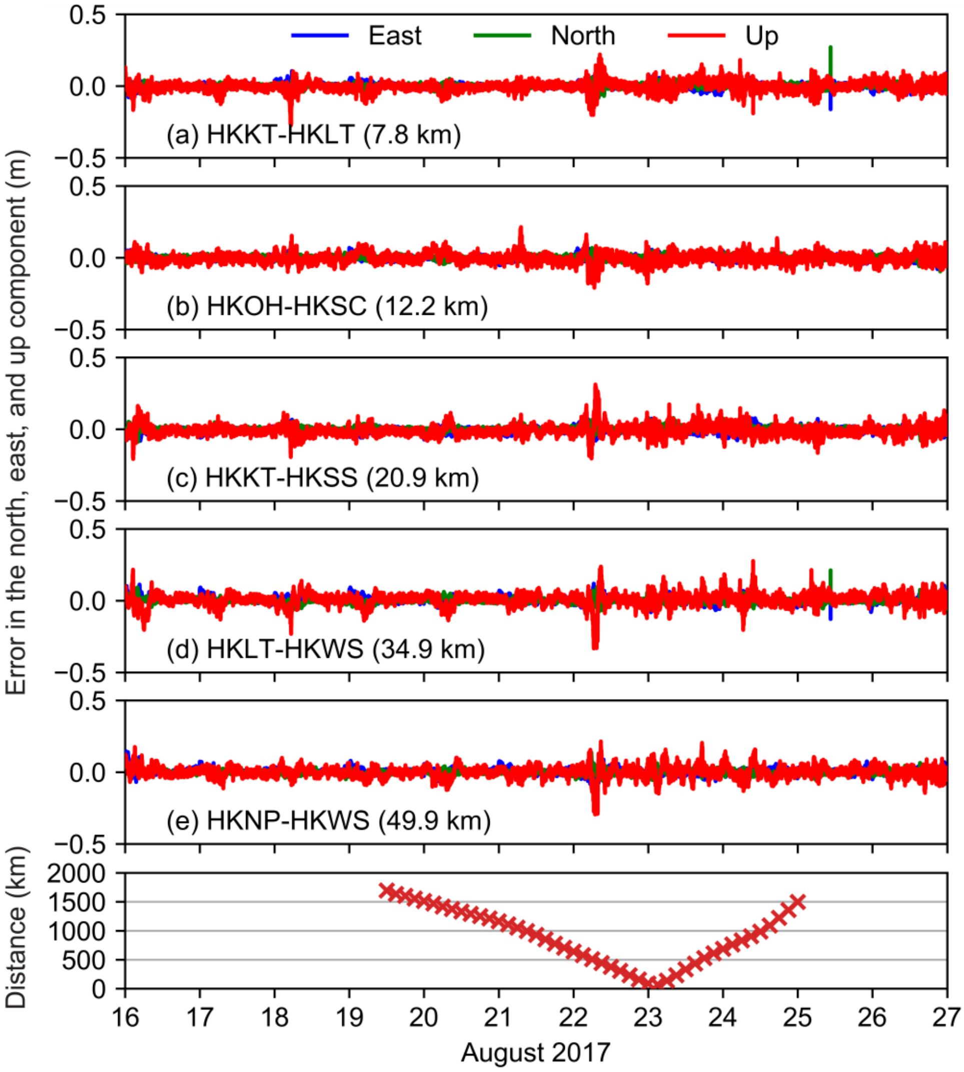

Fig. 5 Positioning errors derived from L3 ionospheric-free observation in the components of the north, east, and up during August 16–26, 2017 for the five baselines: (a) HKKT-HKLT, (b) HKOH-HKSC, (c) HKKT-HKSS, (d) HKLT-HKWS, (e) HKNP-HKWS. The distance between the center of the TC Hato and Hong Kong is shown at the bottom panel.

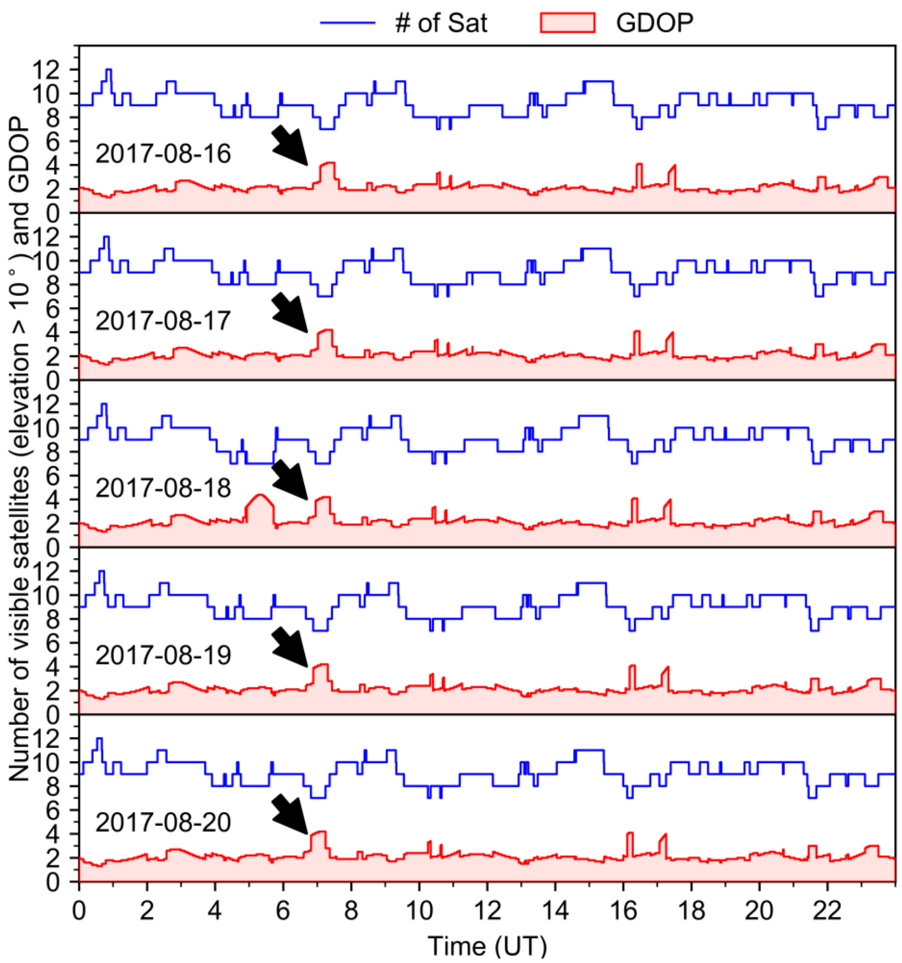

Fig. 6 The number of visible satellites with elevation angle larger than 10° and the corresponding geometric dilution of precision (GDOP) for the Hong Kong region from August 16 - 20, 2017. Fewer visible satellites, i.e., seven satellites, and larger GDOP, i.e., approximately4, showed between 07:00 UT and 08:00 UT every day, which are indicated by the black arrow in each subplot.

The root mean squares (RMS) of the positioning errors in the three-dimension (3D) direction is presented in the top panel of Fig. 7. The largest positioning errors can be observed at around 07:00 UT on August 22 when the TC Hato was 400-600 km from Hong Kong. The positioning errors then decreased when the TC was coming close to Hong Kong. The positioning errors started to increase again when the TC center made landfall near Hong Kong. After the landfall, the positioning performance experienced a slight fluctuation.

We also analyzed the residuals of the ionospheric-free carrier phase measurements. The daily standard deviation of residuals on the ionospheric-free carrier phase measurements is presented in the bottom panel of Fig. 7. The results imply that the TC made a significant impact on GPS measurements. Before the TC started to affect Hong Kong, the residuals were stable with a standard deviation of about 10 mm. When the TC began to hit Hong Kong on August 22, the residuals increased dramatically and the standard deviation reached approximately 16 mm. Afterward, the standard deviation showed a decreasing trend when the TC center made landfall on August 23 and left from Hong Kong on August 24 and August 25.

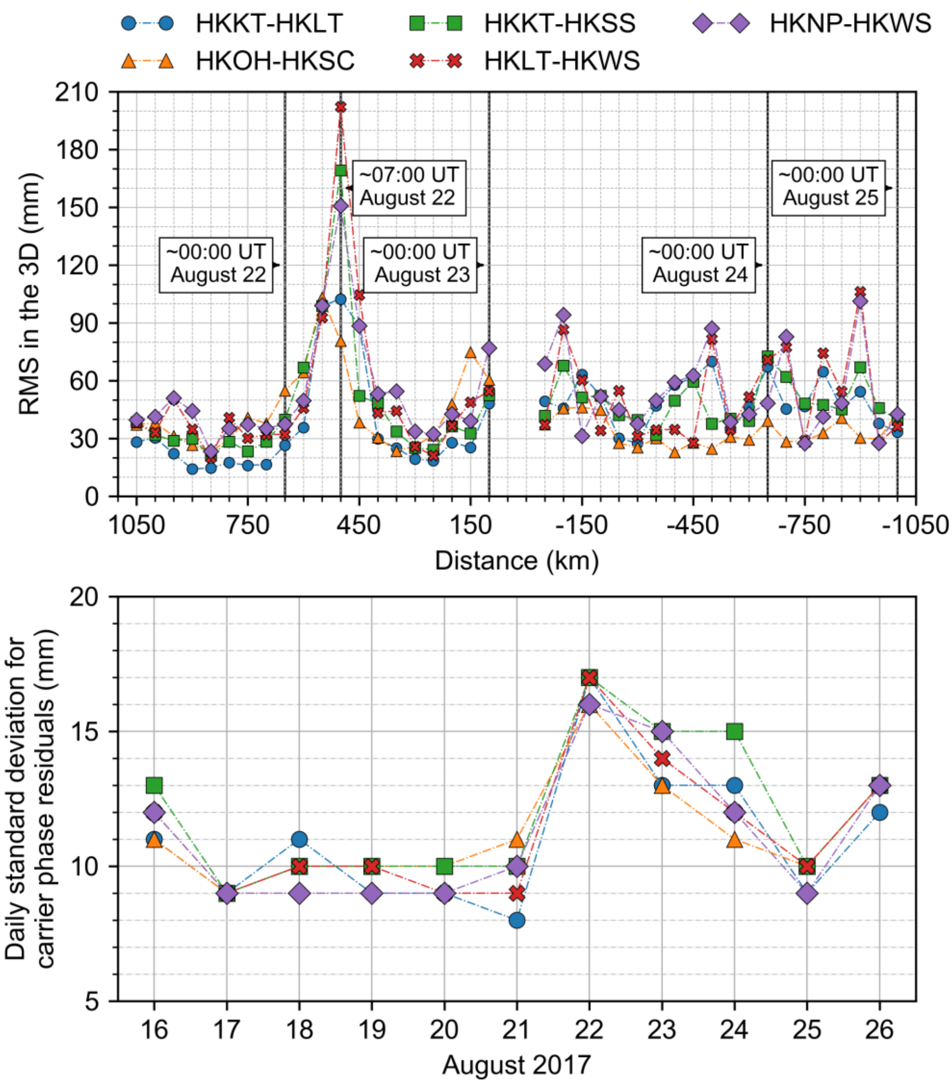

Fig. 7 3D RMS (top) of positioning error against the distance between the TC center and Hong Kong. The positive distance means the TC was approaching Hong Kong, and the negative distance means the TC was departing from Hong Kong. Daily standard deviation (bottom) of residuals on ionospheric-free carrier phase measurements from August 16 to August 26, 2017.

Impact of TC-induced cloud on positioning disturbances on August 22

In this section, the evolution of the cloud with the TC movement is discussed to explain why the significant positioning disturbances occurred on August 22. The cloud distribution near Hong Kong at 00:00 UT, 04:00 UT, and 08:00 UT every day from August 22 to August 24, 2017 is provided in Fig. 8. It is evident that at around 04:00 UT on August 22, Hong Kong was at the edge of the cloud generated by the TC Hato. At that time, the water vapor in the troposphere above Hong Kong was very unpredictable. Lee et al. (2017) demonstrated the spatial distribution of water vapor showed a stripe pattern at the edge of tropical cyclones. Xu and Li (2017) revealed that the landfall area experienced a significant increase in water vapor when the TC Fitow 2013 was about 380 km away. Tang et al. (2018) also showed an uneven distribution of water vapor in the spatial domain at the edge of typhoons.

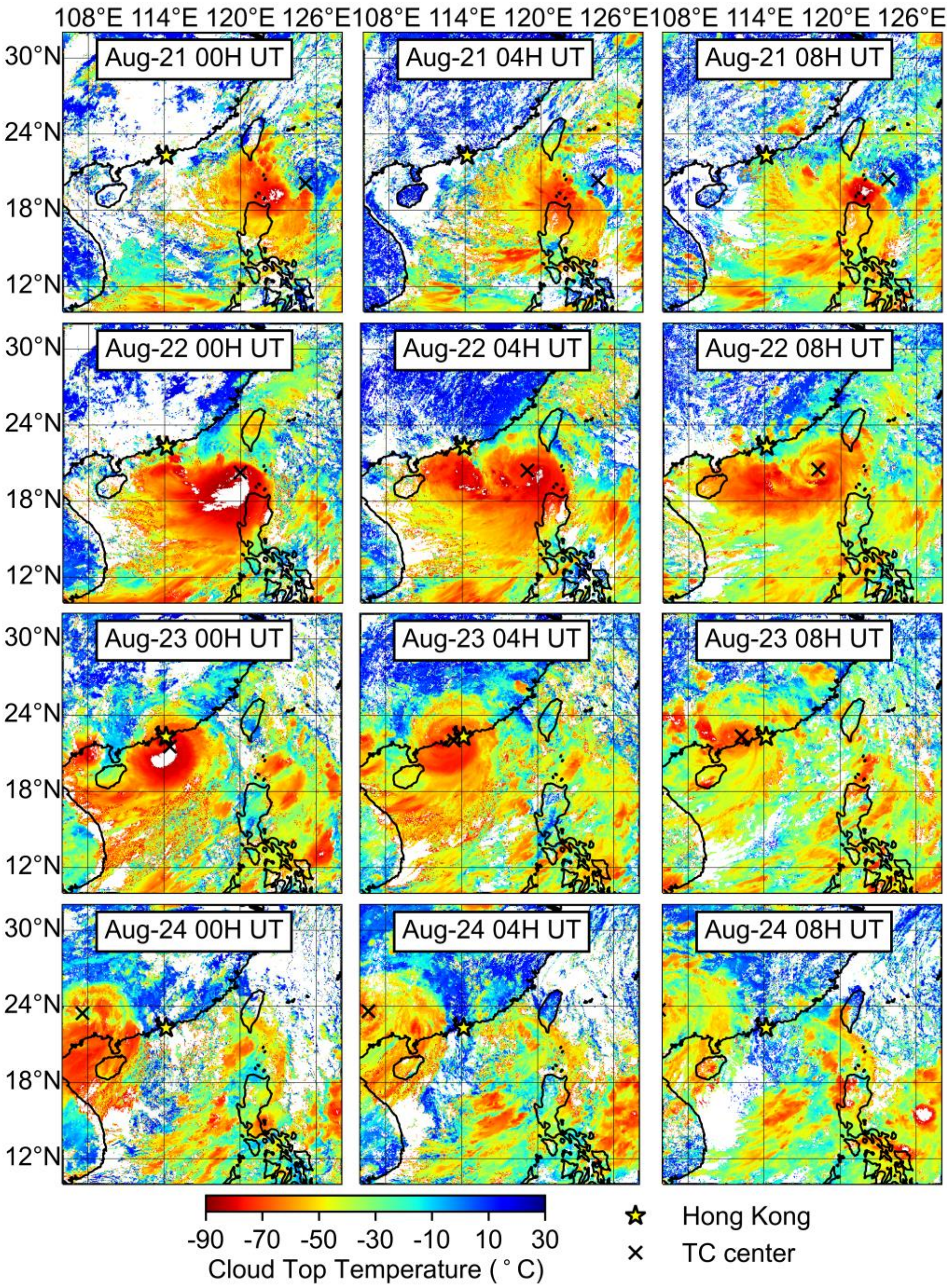

Fig. 8 Cloud top temperature at 00:00 UT, 04:00 UT, and 08:00 UT every day from August 21 to August 24, 1017. The cloud top temperature was retrieved from the Himawari-8 products (https://himawari8.nict.go.jp/). Himawari-8 satellite provided data for daytime only and cloud top

temperature was not observed at nighttime. Thus, cloud top temperature at nighttime was not provided here.

On the other hand, the cloud type above Hong Kong at 04:00 UT on August 22 was cirrus mixed with altocumulus and altostratus, as shown in Fig. 9**Error! Reference source not found.**. At that time, Hong Kong was in the middle of two deep convection bands. The water content in different clouds is comprised of ice water content (IWC) and liquid water content (LWC) with different mixing ratios (Huang et al. 2015; Zhang et al. 2019). Both of them are a major source of water vapor through evaporation (Virts and Houze 2015). Under this condition, the water vapor above Hong Kong had variable characteristics in both temporal and spatial domains. Therefore, it is highly probable that the highly dynamic variation of the water vapor resulted in the positioning disturbances at the beginning of August 22, as shown in Fig. 5**Error! Reference source not found.**.

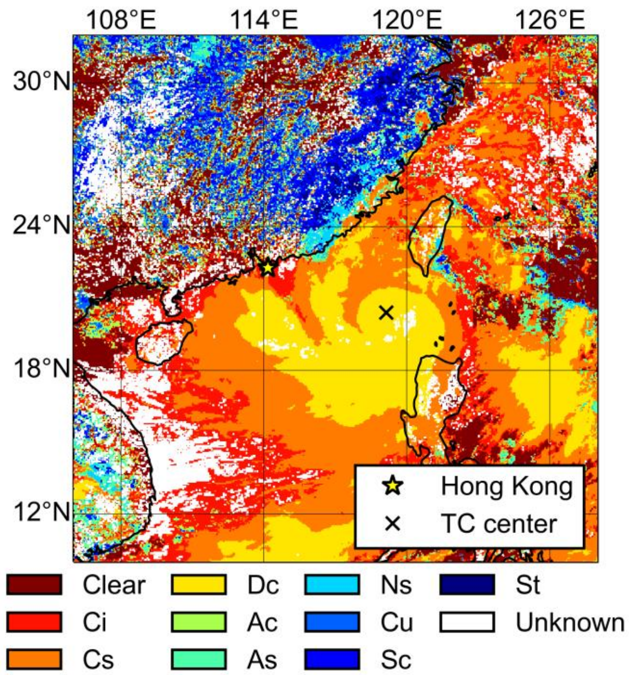

Fig. 9 Cloud types at 04:00 UT on August 22, 2017, retrieved from the Himawari-8 products (https://himawari8.nict.go.jp/). The cloud types are clear, cirrus (Ci), cirrostratus (Cs), deep convection (Dc), altocumulus (Ac), altostratus (As), nimbostratus (Ns), cumulus (Cu), stratocumulus (Sc), stratus (St), and unknown.

Positioning periodical variations induced by Hato on August 22

As shown in Fig. 5**Error! Reference source not found.**, the positioning errors in the up component is much larger than those in horizontal components. This is due to the geometry of the GPS satellites (Santerre and Geiger 2018). Therefore, the following analysis will mainly focus on the positioning results in the up component. An example of the positioning results of the baseline HKKT-HKSS in the frequency domain is shown in Fig. 10. We divide the nine periods mentioned above into two categories: (a) 24.0 h, 12.0 h, 8.0 h, and 6.0 h; (b) 4.8 h, 4.0 h, 3.4 h, 3.0 h, and 2.7 h. The averaged spectrum magnitudes for the periods in category (a) (6.0 h to 24.0 h) are always stronger than those of the periods in category (b) (2.7 h to 4.8 h) except for August 22 and 24, 2017. On August 22, the mean spectrum magnitude, i.e., 41.4 on average, of the periods in category (b) is about 1.3 times as large as the one of the periods in category (a). On August 24, though the spectrum magnitudes of the periods in category (b) are slightly larger than those of the periods in category (a), its magnitudes are similar to those in the other days except August 22.

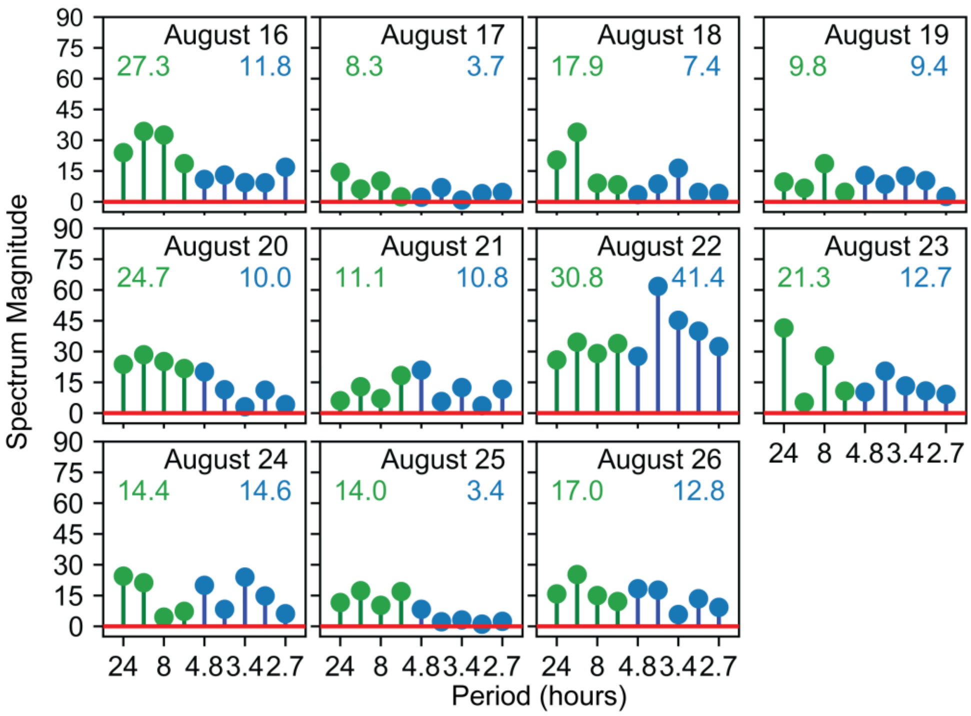

Fig. 10 Spectrum magnitudes with two categories of periods: (a) 24.0 h, 12.0 h, 8.0 h, and 6.0 h in green color; (b) 4.8 h, 4.0 h, 3.4 h, 3.0 h, and 2.7 h in blue color during August 16-26, 2017. The mean value of spectrum magnitudes over categories (a) and (b) periods is shown in green and blue numbers, respectively. The discrete Fourier transform is performed with the positioning errors in the up component for the baseline HKKT-HKSS based on the L3 combination observation.

Furthermore, the daily variation of spectrum magnitude of baseline HKKT-HKSS over each period is provided in Fig. 11. It is obvious to note the spectrum magnitudes of two categories of the period show different variation patterns. The spectrum magnitudes for periods in category (a) (6.0 h to 24.0 h) varied day to day but without an abrupt jump, while the spectrum magnitudes for periods in category (b) (2.7 h to 4.8 h) showed an abrupt jump on August 22. The largest increase occurred at the period of 4.0 h, denoted by the purple triangle. Its spectrum magnitude increased from 5.6 on August 21 to 61.7 on August 22, 2017. The spectrum magnitude then went down to the average level again on August 23, 2017.

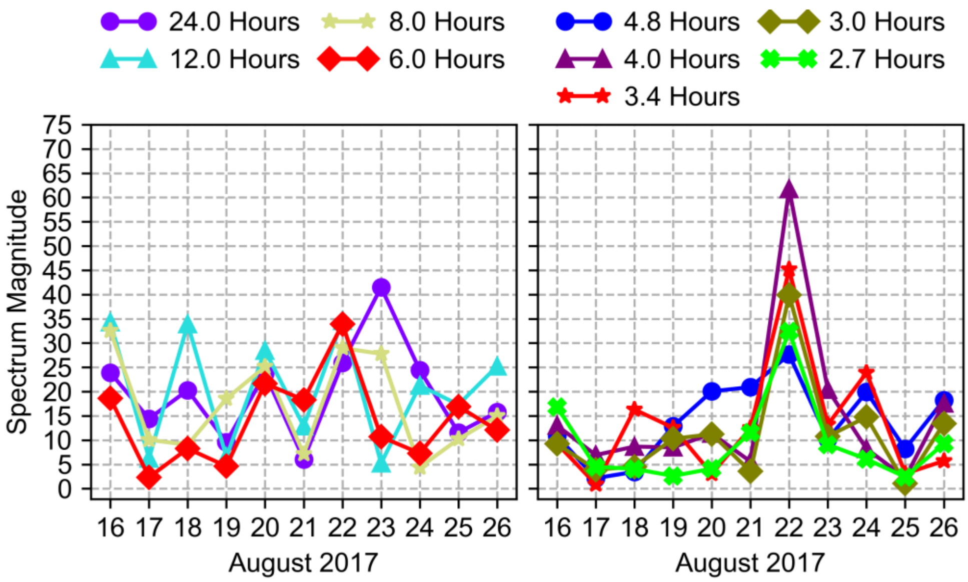

Fig. 11 Daily spectrum magnitudes of discrete Fourier transform of vertical positioning errors of the baseline HKKT-HKSS during the TC period. (left) The magnitude of category (a) periods: 24.0 h, 12.0 h, 8.0 h, and 6.0 h; (right) the magnitude of category (b) periods: 4.8 h, 4.0 h, 3.4 h, 3.0 h, and 2.7 h.

It has been shown on the baseline HKKT-HKSS that the spectrum magnitudes corresponding to category (b) periods are much larger than those of category (a). Therefore, it is necessary to study the spectrum magnitudes corresponding to category (b) periods for all the other baselines. The daily mean spectrum magnitudes for all the five baselines over the periods of category (b) 4.8 h, 4.0 h, 3.4 h, 3.0 h, and 2.7 h are shown in Fig. 12. There is an obvious increase in the spectrum magnitude on August 22 for the baselines HKKT-HKSS, HKLT-HKWS, and HKNP-HKWS, but no large increase is observed for the baselines HKKT-HKLT and HKOH-HKSC. This unnoticeable increase at these two baselines is attributed to the relatively short lengths of the baselines. When the two stations of a baseline have a short separation, their tropospheric effects have a strong correlation (Wielgosz et al.

2011). Most of the tropospheric delays in double-differencing observation can be canceled in short baselines. In comparison, the tropospheric delays above two stations of long baselines are different. It is hard to remove them in double-differencing observation (Tang et al. 2018; Chen et al. 2019). The tropospheric delay residuals are absorbed to the other estimated parameter, e.g., coordinates. Therefore, the variation of the positioning errors is correlated with the variation of the troposphere. The exact impact of the troposphere on the positioning performance will be discussed in the following section.

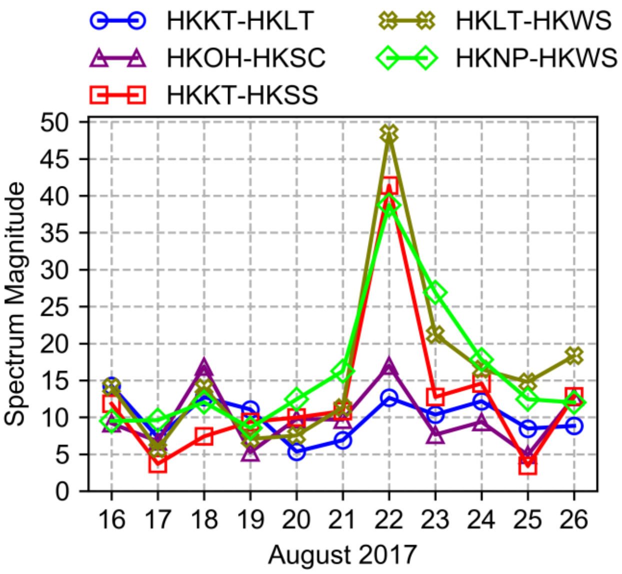

Fig. 12 Average spectrum magnitudes over the periods of 4.8 h, 4.0 h, 3.4 h, 3.0 h, and 2.7 h after the discrete Fourier transform of the vertical component of all the five baselines HKKT-HKLT, HKOH-HKSC, HKKT-HKSS, HKLT-HKWS, and HKNP-HKWS. A significant increase in the average spectrum magnitude is observed on August 22 at the three long baselines HKKT-HKSS, HKLT-HKWS, and HKNP-HKWS with a length of 20.9 km, 34.9 km, and 49.9 km, respectively. The average spectrum magnitude increase is not apparent at HKKT-HKLT and HKOH-HKSC, with a length of 7.8 km and 12.2 km, respectively.

PWV periodical variations induced by Hato on August 22

The relationship between the tropospheric effect and positioning error was discussed in Santerre and Geiger (2018). The relative tropospheric bias, represented by the difference of tropospheric delays between two baseline stations, has a strong correlation with the GPS positioning accuracy in the up component. To investigate the contribution of the relative tropospheric bias on the GPS positioning performance, we estimated the zenith wet delay (ZWD) above every station using GPS PPP processing mode. Then, the precipitable water vapor (PWV) above every station was calculated using the following equation (Yeh et al. 2016):

$$PWV = ZWD \cdot \Pi \tag{3}$$

where Π is the PWV conversion factor, and can be expressed as (Yeh et al. 2016):

$$\Pi = \frac{10^6}{\rho_w R_w (K_2^{'} + K_3 / T_m)} \tag{4}$$

where ρ_w is the density of liquid water in unit of kg/m^3; R_w is the specific gas constant for water vapor; $K_2^{'}$ and K_3 are two atmospheric refractivity constants; T_m is the weighted-mean temperature of the atmosphere in unit of Kelvin, which can be calculated as (Yeh et al. 2016):

$$T_m = \frac{\int_H^{+\infty} \frac{e(h)}{T(h)} dh}{\int_H^{+\infty} \frac{e(h)}{T(h)^2} dh} \tag{5}$$

where H is the height of the station in the unit of meter; $e(h)$ is the water vapor pressure at the given height h in the unit of hPa; $T(h)$ is the absolute temperature at the given height h in the unit of Kelvin; dh in the unit of meter is the increment along the vertical integral path. In this study, the water vapor pressure and temperature were derived from the European Centre for Medium-Range Weather Forecasts (ECMWF) Reanalysis (ERA-Interim) pressure levels products.

Fig. 13 provides the PWV above the GPS stations during the TC period. The PWV above every station followed a similar trend. On August 21, the PWV started to increase rapidly, even if Hato was still about 1,200 km away from Hong Kong. With Hato moving towards Hong Kong, the PWV experienced a fluctuating pattern. It peaked at about 75 kg/m^2 in the early morning on August 23 when the TC center made landfall near Hong Kong. After the TC Hato left Hong Kong, the PWV showed a sharp reduction.

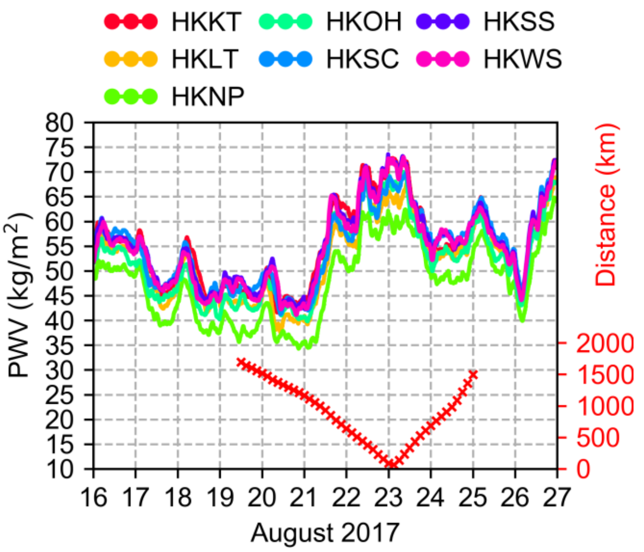

Fig. 13 Precipitable water vapor over the GPS stations along with the distance between Hato and Hong Kong during the TC period, August 16-27, 2017.

To study the variation of the PWV over each baseline, we performed a continuous wavelet spectral analysis on the differenced PWV between two baseline stations. The detailed implementation of continuous wavelet analysis has been discussed by Torrence and Compo (1998) and Liu et al. (2007). Differenced PWV has a low temporal resolution, i.e. 15 mins. The periods cannot be well captured using the discrete Fourier transform. Thus, we performed a continuous wavelet spectral analysis on the differenced PWV between two baseline stations. Fig. 14 provides an example of the wavelet spectral result on differenced PWV of the baseline HKKT-HKSS (baseline length 20.9 km). The wavelet power spectra were calculated based on the detrended PWV difference, represented as the red curve in the top panel. The wavelet power spectra are provided in the middle panel. It is clear to see that on August 22, 2017, there is a strong power for the periods from 2.0 h to 5.0 h, as marked in a red circle. In addition, the scale-averaged wavelet power over the periods of 2-5 h is shown in the bottom panel. Correspondingly, the averaged power showed a distinct variation on August 22, 2017.

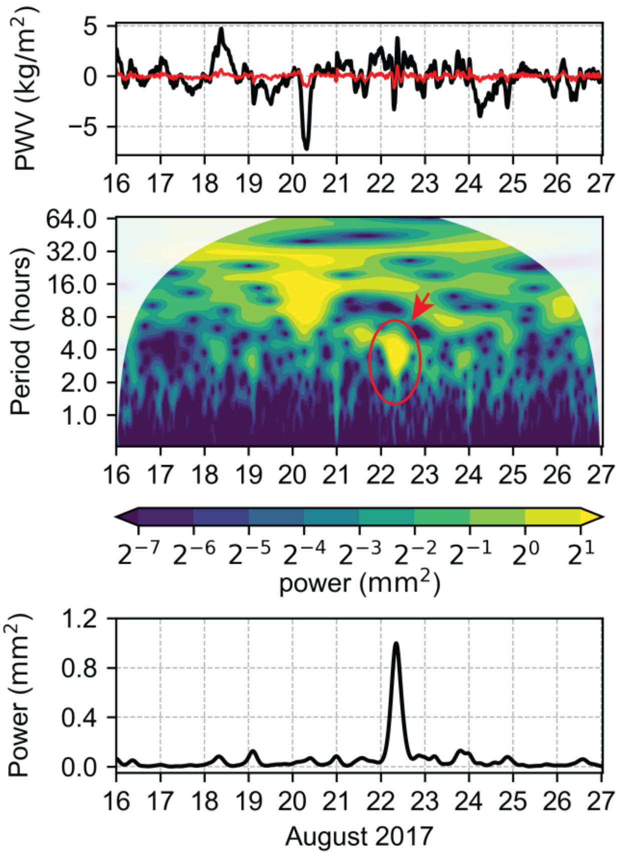

Fig. 14 Continuous wavelet spectrum analysis of the differenced PWV for the baseline HKKT-HKSS (baseline length 20.9 km). (top) The time series of the original PWV difference is shown in black and the detrended PWV difference is shown in red; (middle) the wavelet power spectra; (bottom) the scale-averaged wavelet power over the 2-5 h time scale.

Fig. 15 represents the 2-5 h scale-averaged wavelet power for all the five baselines. The averaged powers for the two short baselines HKKT-HKLT (7.8 km in length) and HKOH-HKSC (12.2 km) are low with a mean of 0.028 and 0.036, respectively. Their maxima are 0.268 and 0.290, respectively. By comparison, the averaged power shows a significant increase on August 22, with peak values of 0.998, 1.230, and 1.303 for the baselines HKKT-HKSS, HKLT-HKWS, and HKNP-HKWS, respectively. The baselines HKKT-HKSS, HKLT-HKWS, and HKNP-HKWS have a length of 20.9 km, 34.9 km, and 49.9 km, respectively. The peak values increase with the increase of baseline length.

It is worth noting that the periods of differenced PWV variation have a good agreement with those of GPS positioning errors (in the up component) discussed in the above section. PWV with distinct variations have a period range of 2 h to 5 h. The vertical positioning errors with large spectrum magnitudes have periods of 2.7 h, 3.0 h, 3.4 h, 4.0 h, and 4.8 h. Such a good agreement implies that the periodical tropospheric PWV variation induced by the TC Hato resulted in positioning variations with the periods of 2-5 h.

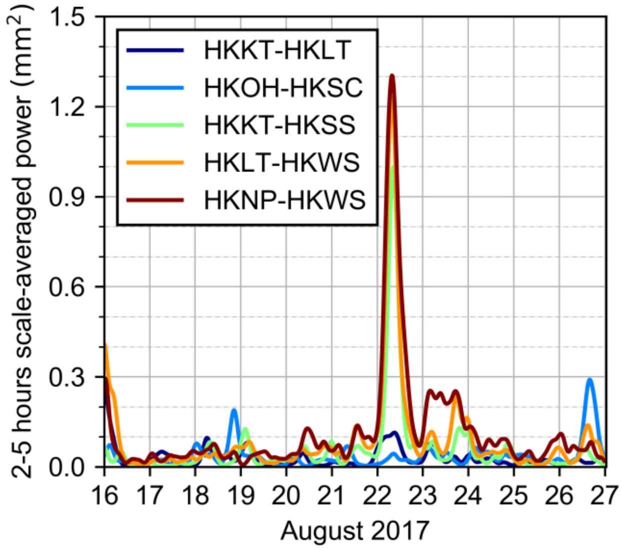

Fig. 15 2-5 h scale-averaged wavelet power of the differenced PWV for all the five baselines. On August 22, 2017, the peak power values were 0.998, 1.230, and 1.303 for the three long baselines HKKT-HKSS (20.9 km), HKLT-HKWS (34.9 km), and HKNP-HKWS (49.9 km), respectively. On the same day, the peak power values of HKKT-HKLT (7.8 km) and HKOH-HKSC (12.2 km) are low, with a mean of 0.028 and 0.036, respectively.

PWV periodical variations due to spiral rainbands

The PWV periodical variation is considered to attribute to the spiral rainbands around the TC center. Atkinson (1971) found that the spiral rainbands often had a width of 20-40 km. In addition, the translation speed of TCs was tens of kilometers on average. Therefore, the atmosphere had a periodical characteristic in the radial direction of TCs. The image of radar echoes at 11:00 UT (19:00 LT) on August 22 is presented in Fig. 16. Three rainbands can be observed with a width of around55 km, 30 km, and 45 km, respectively. The separations among the three rainbands are about 50 km and 30 km. Furthermore, the translation speed of Hato was approximately 25 km/h at that time. Thus, it took about 4.2 hours ((55 km + 50 km)/25 km/h) before the second rainband hit Hong Kong. Similarly, it took about 2.4 hours before the third rainband arrived in Hong Kong. The period is consistent with that derived from GPS positioning results and the differenced PWV.

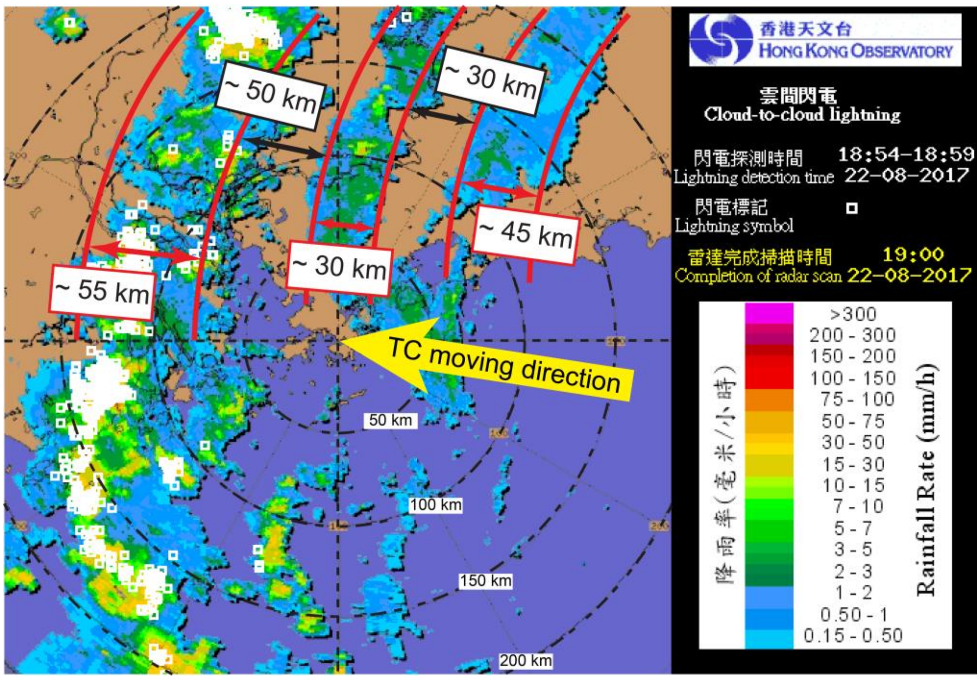

Fig. 16 Image of radar echoes at 11:00 UT (19:00 LT) on August 22, 2017 (image source: Hong Kong Observatory, obtainable from the Atmospheric and Environmental Database, hosted by the Environmental Central Facility, the Hong Kong University of Science and Technology, http://cozumel.ust.hk/dataview/hko_radar/current/).

Zenith hydrostatic delay variation during the Hato period

In addition to the wet tropospheric delays, the hydrostatic part is another error source in the GPS positioning, accounting for approximately 90% of the total tropospheric delay (Chen and Liu 2016). In this part, we investigated the zenith hydrostatic delays at each GPS station during the TC period. The zenith hydrostatic delays can be expressed as (Saastamoinen 1972):

$$ZHD = 0.0022793 \cdot \frac{P_s}{f(\varphi, H)} \tag{6}$$

$$f(\varphi, H) = 1 - 0.0026 \cdot \cos(2\varphi) - 2.8 \times 10^{-7} \cdot H \tag{7}$$

where P_s is the surface pressure in the unit of hPa; φ is the GPS station latitude in the unit of radians and H is the height of the GPS station above sea level in the unit of meters.

The hydrostatic delay in the zenith direction at each station is presented inFig. 17. Compared with the PWV variation, as shown Fig. 13, ZHD varied more smoothly during the TC period. ZHD at

HKKT, HKOH, HKSS, and HKWS stations showed an evident decreasing trend while the TC Hato was approaching Hong Kong. Then, ZHD at the four stations returned to an average value after the TC's landfall.

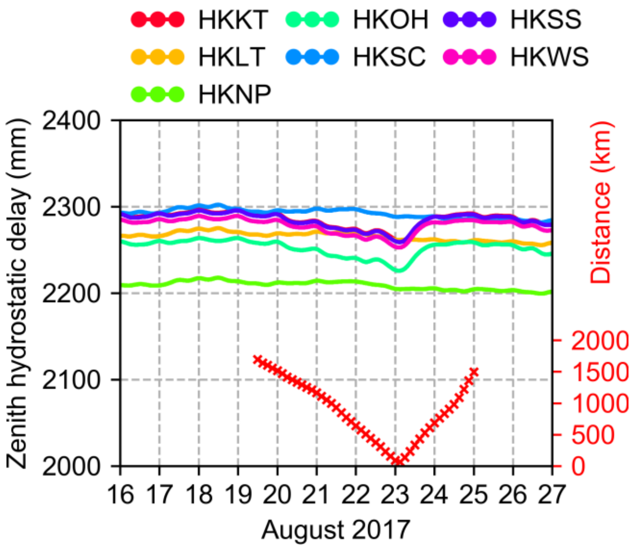

Fig. 17 Zenith hydrostatic delay over the GPS stations along with the distance between Hato and Hong Kong during the TC period, August 16-27, 2017.

Furthermore, we applied the continuous wavelet spectral analysis on the differenced ZHD over different baselines. Fig. 18 represents the 2-5 h scale-averaged wavelet power of the differenced ZHD over all the five baselines. Compared with the results of the differenced PWV, an evident increase was shown on August 22 in Fig. 15, the wavelet power of the differenced ZHD did not experience such a distinct variation during the TC period. Besides, the 2-5 h scale-averaged wavelet power of the differenced ZHD had much smaller values, less than 0.002, than that of the differenced PWV. In short, our analysis showed that the periodical variation hiding in the positioning error on August 22 was caused by the periodical variation of the wet part in the troposphere delays, i.e. PWV.

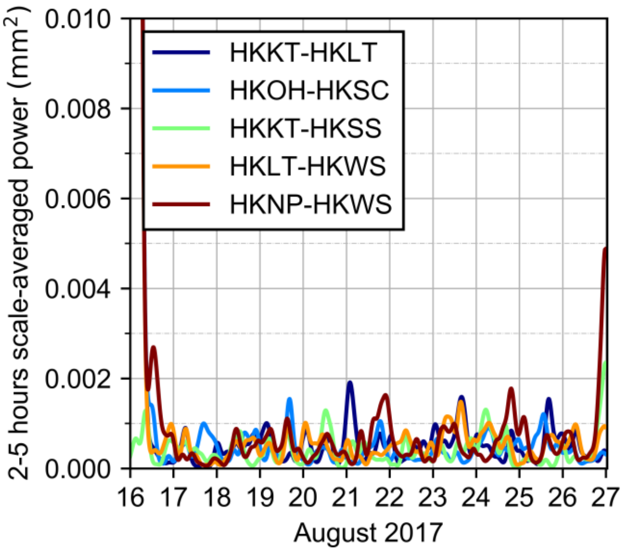

Fig. 18 2-5 h scale-averaged wavelet power of the differenced ZHD over all the five baselines.

Potential methods to mitigate tropospheric periodical variation

In order to mitigate the tropospheric effect under extreme weather conditions, a number of efforts have been made. For instance, Hobiger et al. (2010) proposed a fine-mesh numerical weather model for GPS tropospheric corrections. Their results showed that the vertical positioning performance could be improved by up to 30% during the 2007 typhoon Fitow period. Wilgan and Geiger (2018) presented high-resolution (i.e. 1.1 km × 1.1 km) models of tropospheric corrections for the Alpine area in Switzerland. The zenith total delay from their models had a good agreement with that from the GNSS-based model, with average bias and standard deviation of 0.2 mm and 4.3 mm, respectively.

Furthermore, the prediction models of tropospheric correction based on machine learning algorithms were discussed by Zhang et al. (2020) and Selbesoglu (2020). In their studies, the prediction models can forecast tropospheric corrections six hours in advance. The prediction accuracy of the tropospheric corrections was in the range of 7.2 mm to 15.0 mm. These models can be utilized to mitigate the tropospheric effect during the TC's approach. However, the model performance should be further assessed under different severe weather conditions in different geographical regions.

Concluding Remarks

The passage of the TC Hato (1713) resulted in severe positioning disturbances to GPS baseline solutions in the Hong Kong region. When the TC approached Hong Kong at a distance of 400-600 km on August 22, the RMS of positioning errors in the 3D component suddenly increased from about

30 mm to 140 mm. Then, the RMS decreased to the average level, i.e., about 30 mm, while the TC continued to move towards Hong Kong. The RMS increased again to about 70 mm when the TC center passed by Hong Kong.

After applying the discrete Fourier transform to the GPS positioning errors in the up component, we investigated the spectrum magnitudes of nine frequencies lower than 11.6×10^{-5} Hz. The results showed that the primary frequencies in vertical positioning errors are 10.4×10^{-5} Hz, 9.26×10^{-5} Hz, 8.10×10^{-5} Hz, 6.94×10^{-5} Hz, and 5.79×10^{-5} Hz, which corresponds to the periods of 2.7 h, 3.0 h, 3.4 h, 4.0 h, and 4.8 h, respectively. The mean spectrum magnitudes over the five periods for the baselines HKKT-HKLT, HKOH-HKSC, HKKT-HKSS, HKLT-HKWS, and HKNP-HKWS on August 22, 2017 are 1.30, 1.84, 4.28, 3.71, and 2.82 times as large as the ones on other days from August 16 to August 26, 2017. The increase of spectrum magnitude of these periods is particularly large for the long baselines (20.9 km or longer) i.e., HKKT-HKSS, HKLT-HKWS, and HKNP-HKWS, on August 22, 2017.

Examining the differenced PWV and ZHD between two baseline stations via the continuous wavelet spectral analysis, we found that the periodical variation of the positioning results was caused by the wet part of the tropospheric delays. The differenced PWV between the two stations of long baselines (HKKT-HKSS, HKLT-HKWS, and HKNP-HKWS) was found to have periods of 2-5 hours on August 22, 2017. The 2-5 hours scale-averaged power on that day reached peak values of 0.998, 1.230, and 1.303 for the HKKT-HKSS, HKLT-HKWS, and HKNP-HKWS baselines, respectively, much larger than the normal level < 0.1.

The periods of differenced PWV variation on August 22, 2017 have a good agreement with those of spiral rainbands in the TC. On the other hand, the periods of differenced PWV variation are consistent with those of large magnitudes in the positioning errors. The findings indicate that the PWV above the Hong Kong region experienced a variation with the period of 2-5 hours when the TC started to affect the Hong Kong region. Consequently, the GPS positioning solutions was degraded with errors of the same periods.

Acknowledgment

The grant support from the Key Program of the National Natural Science Foundation of China (project No.: 41730109) is acknowledged. The grant supports from the Hong Kong Research Grants Council (RGC) projects (B-Q61L PolyU 152222/17E) are highly appreciated. The support from the project (No. 1-BBWJ) in the Emerging Frontier Area (EFA) Scheme of the Research Institute for Sustainable Urban Development (RISUD) of The Hong Kong Polytechnic University is also acknowledged.

Data Availability

The Lands Department of the Government (https://www.geodetic.gov.hk/en/rinex/downv.aspx) of Hong Kong Special Administrative Region (HKSAR) provided the GPS data from the Hong Kong Satellite Positioning Reference Station Network (SatRef). The Hong Kong Observatory provided the image of radar echoes (http://cozumel.ust.hk/dataview/hko_radar/current/). The International GNSS Service (IGS) provided the daily precise orbit and clock GPS products from the ftp address ftp://cddis.gsfc.nasa.gov/gps/products/ during the period of August 16-26 2017. The National Oceanic and Atmospheric Administration (NOAA) provided the International Best Track Archive for Climate Stewardship (IBTrACS) data on tropical cyclones (https://www.ncei.noaa.gov/data/international-best-track-archive-for-climate-stewardship-ibtracs/v04r00/access/csv/). In addition, we also would like to thank the Japan Aerospace Exploration Agency (JAXA) (https://www.eorc.jaxa.jp/ptree/userguide.html) for providing the Himawari-8 L1 gridded data. The European Centre for Medium-Range Weather Forecasts (ECMWF) provided the data set of ECMWF atmospheric reanalysis of the global climate (ERA-Interim), which is available on the website https://apps.ecmwf.int/datasets/data/interim-full-daily/levtype=sfc/.

The data used in this study have been uploaded to the public domain repository Figshare, which is a free data repository open to the public. The daily GPS data in the format of Receiver Independent Exchange Format (RINEX) 2.11 during the period from August 16-26, 2017 can be download from https://doi.org/10.6084/m9.figshare.12799943.v1. The precise daily orbit (sp3) and clock (clk_30s) GPS products are available from https://doi.org/10.6084/m9.figshare.12799949.v1. The records of the tropical cyclone Hato (1713) are available at https://doi.org/10.6084/m9.figshare.12781820.v1. The Himawari-8 image at 04:00 UT on August 22, 2017 can be downloaded from https://doi.org/10.6084/m9.figshare.12799931.v1. The water vapor pressure and temperature of ERA-Interim hourly data on pressure levels ranging from 21 N to 26 N and 112 E to 123 E in latitude and longitude in August 2017 can be found at https://doi.org/10.6084/m9.figshare.12799964.v1.

References

Atkinson GD (1971) Forecaster's guide to tropical meteorology. United States Air Force, Air Weather Service

Calori A, Santos JR, Blanco M, Pessano H, Llamedo P, Alexander P, de la Torre A (2016) Ground-based GNSS network and integrated water vapor mapping during the development of severe storms at the Cuyo region (Argentina). Atmospheric Res 176–177:267–275. https://doi.org/10.1016/j.atmosres.2016.03.002

Chen B, Liu Z (2016) A Comprehensive Evaluation and Analysis of the Performance of Multiple Tropospheric Models in China Region. IEEE Trans Geosci Remote Sens 54(2):663–678. https://doi.org/10.1109/TGRS.2015.2456099

Chen B, Liu Z, Wong W-K, Woo W-C (2017) Detecting Water Vapor Variability during Heavy Precipitation Events in Hong Kong Using the GPS Tomographic Technique. J Atmospheric Ocean Technol 34(5):1001–1019. https://doi.org/10.1175/jtech-d-16-0115.1

Chen D, Ye S, Xu C, Jiang W, Jiang P, Chen H (2019) Undifferenced zenith tropospheric modeling and its application in fast ambiguity recovery for long-range network RTK reference stations. GPS Solut 23(1):26. https://doi.org/10.1007/s10291-018-0815-x

Dach R, Lutz S, Walser P, Fridez P (2015) Bernese GNSS Software version 5.2. User manual, Astronomical Institute, University of Bern, Bern Open Publishing

Hobiger T, Shimada S, Shimizu S, Ichikawa R, Koyama Y, Kondo T (2010) Improving GPS positioning estimates during extreme weather situations by the help of fine-mesh numerical weather models. J Atmospheric Sol-Terr Phys 72(2):262–270. https://doi.org/10.1016/j.jastp.2009.11.018

Hong Kong Observatory (2019) Tropical Cyclones in 2017. Hong Kong Observatory, Hong Kong

Huang L, Jiang JH, Wang Z, Su H, Deng M, Massie S (2015) Climatology of cloud water content associated with different cloud types observed by A-Train satellites. J Geophys Res Atmospheres 120(9):4196–4212. https://doi.org/10.1002/2014JD022779

Knapp KR, Kruk MC, Levinson DH, Diamond HJ, Neumann CJ (2010) The International Best Track Archive for Climate Stewardship (IBTrACS). Bull Am Meteorol Soc 91(3):363–376. https://doi.org/10.1175/2009BAMS2755.1

Lee Y-K, Li J, Li Z, Schmit T (2017) Atmospheric temporal variations in the pre-landfall environment of typhoon Nangka (2015) observed by the Himawari-8 AHI. Asia-Pac J Atmospheric Sci 53(4):431–443. https://doi.org/10.1007/s13143-017-0046-z

Li B, Feng Y, Shen Y, Wang C (2010) Geometry-specified troposphere decorrelation for subcentimeter real-time kinematic solutions over long baselines. J Geophys Res Solid Earth 115(B11). https://doi.org/10.1029/2010JB007549

Liu Y, San Liang X, Weisberg RH (2007) Rectification of the Bias in the Wavelet Power Spectrum. J Atmospheric Ocean Technol 24(12):2093–2102. https://doi.org/10.1175/2007JTECHO511.1

Marks FD (2015) Tropical Cyclones And Hurricanes | Hurricanes: Observation. In: North GR, Pyle J, Zhang F (eds) Encyclopedia of Atmospheric Sciences (Second Edition). Academic Press, Oxford, pp 35–56

Saastamoinen J (1972) Atmospheric correction for the troposphere and stratosphere in radio ranging satellites. Use Artif Satell Geod :247–251. https://doi.org/10.1029/GM015p0247

Santerre R, Geiger A (2018) Geometry of GPS relative positioning. GPS Solut 22(2):50–50. https://doi.org/10.1007/s10291-018-0713-2

Selbesoglu MO (2020) Prediction of tropospheric wet delay by an artificial neural network model based on meteorological and GNSS data. Eng Sci Technol Int J 23(5):967–972. https://doi.org/10.1016/j.jestch.2019.11.006

Strang G (1994) Wavelets. Am Sci 82(3):250–255

Tang W, Shen M, Deng C, Cui J, Yang J (2018) Network-based triple-frequency carrier phase ambiguity resolution between reference stations using BDS data for long baselines. GPS Solut 22(3):73. https://doi.org/10.1007/s10291-018-0737-7

Torrence C, Compo GP (1998) A Practical Guide to Wavelet Analysis. Bull Am Meteorol Soc 79(1):61–78. https://doi.org/10.1175/1520-0477(1998)079<0061:APGTWA>2.0.CO;2

Tunalı E, Özlüdemir MT (2019) GNSS PPP with different troposphere models during severe weather conditions. GPS Solut 23(3):82. https://doi.org/10.1007/s10291-019-0874-7

Virts KS, Houze RA (2015) Clouds and Water Vapor in the Tropical Tropopause Transition Layer over Mesoscale Convective Systems. J Atmospheric Sci 72(12):4739–4753. https://doi.org/10.1175/JAS-D-15-0122.1

Wielgosz P, Paziewski J, Baryła R (2011) On Constraining Zenith Tropospheric Delays in Processing of Local GPS Networks with Bernese Software. Surv Rev 43(323):472–483. https://doi.org/10.1179/003962611X13117748891877

Wilgan K, Geiger A (2018) High-resolution models of tropospheric delays and refractivity based on GNSS and numerical weather prediction data for alpine regions in Switzerland. J Geod 93(6):819–835. https://doi.org/10.1007/s00190-018-1203-6

Wilgan K, Hadas T, Hordyniec P, Bosy J (2017) Real-time precise point positioning augmented with high-resolution numerical weather prediction model. GPS Solut 21(3):1341–1353. https://doi.org/10.1007/s10291-017-0617-6

Xu H, Li X (2017) Torrential rainfall processes associated with a landfall of Typhoon Fitow (2013): A three-dimensional WRF modeling study. J Geophys Res Atmospheres 122(11):6004–6024. https://doi.org/10.1002/2016JD026395

Yeh T-K, Hong J-S, Wang C-S, Chen C-H, Chen K-H, Fong C-T (2016) Determining the precipitable water vapor with ground-based GPS and comparing its yearly variation to rainfall over Taiwan. Adv Space Res 57(12):2496–2507. https://doi.org/10.1016/j.asr.2016.04.002

Zhang D, Zhang J, Yao F, Shi L (2019) Observed Characteristics Change of Tropical Cyclones During Rapid Intensification Over Western North Pacific Using CloudSat Data. IEEE J Sel Top Appl Earth Obs Remote Sens 12(6):1725–1733. https://doi.org/10.1109/JSTARS.2019.2917091

Zhang Q, Li F, Zhang S, Li W (2020) Modeling and Forecasting the GPS Zenith Troposphere Delay in West Antarctica Based on Different Blind Source Separation Methods and Deep Learning. Sensors 20(8). https://doi.org/10.3390/s20082343

Zheng F, Lou Y, Gu S, Gong X, Shi C (2018) Modeling tropospheric wet delays with national GNSS reference network in China for BeiDou precise point positioning. J Geod 92(5):545–560. https://doi.org/10.1007/s00190-017-1080-4

Author Biographies

Shiwei Yu is currently a Ph.D. candidate at the Hong Kong Polytechnic University, Hong Kong, China. He received the B.S. and M.S. degrees in Surveying Engineering from China University of Mining & Technology, Beijing, China, in 2013 and 2016. His research interests include GNSS data processing.

Zhizhao Liu is currently a Professor at the Department of Land Surveying and Geo-Informatics, Hong Kong Polytechnic University, Hong Kong. His research interests include new algorithm development for precise GNSS positioning and navigation, GNSS precise point positioning, ionosphere and troposphere observation and modeling, and GNSS meteorology. He received B.Sc. from Jiangxi University of Science and Technology, China, in 1994; M.Sc. from Wuhan University, China, in 1997; and a Ph.D. degree from the University of Calgary, Canada, in 2004.